Eur. Phys. J. C 47, 337–346 (2006)
Digital Object Identifier (DOI) 10.1140/epjc/s2006-02582-x

THE EUROPEAN PHYSICAL JOURNAL C

A search for $\mu - e$ conversion in muonic gold

The SINDRUM II Collaboration

W. Bertl[1], R. Engfer[2], E.A. Hermes[2], G. Kurz[2], T. Kozlowski[3], J. Kuth[4], G. Otter[4], F. Rosenbaum[1], N.M. Ryskulov[1], A. van der Schaaf[2], P. Wintz[4], I. Zychor[3]

[1] Paul Scherrer Institut, Villigen, Switzerland
[2] Physik-Institut der Universität Zürich, Zurich, Switzerland
[3] IPJ Swierk, Swierk, Poland
[4] RWTH Aachen, Aachen, Germany

Received: 13 April 2006 /
Published online: 30 May 2006 –

Abstract. We report on a search for $\mu - e$ conversion in muonic gold performed with the SINDRUM II spectrometer at PSI. The measurement resulted in $\Gamma(\mu^- \mathrm{Au} \to \mathrm{e}^- \mathrm{Au}_{\mathrm{g.s.}})/\Gamma_{\mathrm{capture}}(\mu^- \mathrm{Au}) < 7 \times 10^{-13}$ (90% C.L.).

PACS. 13.35.Bv; 13.60.-r; 36.10.-k; 36.10.Dr

1 Introduction

Mixing of leptonic states with different family number as observed in neutrino oscillations [1] does not necessarily imply measurable branching ratios for lepton family-number violating (LFV) processes involving the charged leptons. In the standard model (SM) the conservation of lepton family number follows directly from the assumption of vanishing neutrino masses. In the minimal extension of the model neutrino oscillations are associated with non-diagonal elements of the neutrino mixing matrix in close analogy to the well-known quark mixing matrix even when the numerical patterns of the two matrices are totally different. The rates of LFV decays are suppressed relative to the dominant family-number conserving modes by a factor $(\delta m_\nu / m_W)^4$ which results in branching ratios which are out of reach experimentally. Note that a similar family changing quark decay such as $b \to s\gamma$ does obtain a very significant branching ratio of $O(10^{-4})$ due to the large top mass.

In almost any further extension to the standard model such as supersymmetry, grand unification or extra dimensions additional sources of LFV appear. See [2–5] for reviews. For each scenario a large number of model calculations can be found in the literature with predictions that may well be accessible experimentally. Improved searches for charged LFV thus may either reveal physics beyond the SM or at least lead to a significant reduction in parameter space allowed for such exotic contributions. Charged LFV processes, i.e. transitions between e, μ, and τ, might be found in the decay of almost any weakly decaying particle. Searches have been performed in μ, τ, π, K, B, D, W and Z decay [6]. Whereas highest experimental sensitivities were reached in dedicated μ and K experiments, τ decay starts to become interesting as well [7–9].

LFV muon decays include the purely leptonic modes $\mu^+ \to e^+\gamma$ [10] and $\mu^+ \to e^+e^+e^-$ [11], as well as the semi-leptonic $\mu - e$ conversion in muonic atoms. Whereas the more fashionable models favor $\mu^+ \to e^+\gamma$, this mode has a serious disadvantage from an experimental point of view since the sensitivity is limited by accidental $e^+\gamma$ coincidences and muon beam intensities have to be reduced now already. Searches for $\mu - e$ conversion, at the other hand, are limited by the available beam intensities and large improvements in sensitivity may still be achieved.

Although theoretical predictions generally depend on numerous unknown parameters these uncertainties tend to cancel in the relative strengths of these modes. Once LFV in the charged lepton sector would be found the combined information from many different experiments would allow us to discriminate between the various interpretations.

In this paper we describe the final experiment performed with SINDRUM II, a magnetic spectrometer built especially for the search for $\mu - e$ conversion. Data taking took place at PSI in the year 2000 and preliminary results have been presented at various conferences [12, 13].

2 General considerations

When negatively charged muons stop in matter they quickly form muonic atoms which reach their ground states in a time much shorter than the life time of the atom. Muonic atoms decay mostly through muon decay in orbit (MIO) $\mu^-(A,Z) \to e^- \nu_\mu \overline{\nu}_e (A,Z)$ and nuclear muon cap-

ture (MC) $\mu^-(A,Z) \to \nu_\mu(A,Z-1)^*$ which in lowest order may be interpreted as the incoherent sum of elementary $\mu^- p \to n\nu_\mu$ captures. The MIO rate decreases slightly for increasing values of Z (down to 85% of the free muon rate in the case of muonic gold) due to the increasing muon binding energy. The MC rate at the other hand increases roughly proportional to Z^4. The two processes have about equal rates around $Z = 12$. In the case of muonic gold a capture probability of 97.17(2)% can be deduced from the observed 72.6(5) ns lifetime of the atom [14]. As will be discussed in Sect. 2.2 below both decay and capture processes are potential sources of background in a search for $\mu - e$ conversion.

2.1 $\mu - e$ Conversion in muonic atoms

When the hypothetical $\mu - e$ conversion leaves the nucleus in its ground state the nucleons act coherently which boosts the process relative to the incoherent processes with exited final states. The resulting Z dependence has been studied by several authors [15–18]. For $Z \lesssim 40$ all calculations predict a conversion probability relative to the MC rate which follows the linear rise with Z expected naively. The predictions may, however, deviate by factors 2–3 at higher Z values.

As a result of the two-body final state the electrons produced in $\mu - e$ conversion are mono-energetic and their energy is given by:

$$E_{\mu e} = m_\mu c^2 - B_\mu(Z) - R(A)\,, \qquad (1)$$

where $B_\mu(Z)$ is the atomic binding energy of the muon and $R(A)$ is the atomic recoil energy for a muonic atom with atomic number Z and mass number A. In first approximation $B_\mu(Z) \propto Z^2$ and $R(A) \propto A^{-1}$. For muonic gold $B_\mu = 10.08\,\mathrm{MeV}$ and $R = 0.025\,\mathrm{MeV}$ give $E_{\mu e} = 95.56\,\mathrm{MeV}$.

2.2 Muon induced background

Muon decay in orbit (MIO) constitutes an intrinsic background source which can only be suppressed with sufficient electron energy resolution. The process predominantly results in electrons with energy E_{MIO} below $m_\mu c^2/2$, the kinematic endpoint in free muon decay, with a steeply falling high-energy component reaching up to $E_{\mu e}$. By using a magnetic spectrometer the vast majority of MIO electrons can be kept away from the tracking detectors still maintaining a $\approx 50\%$ acceptance in the region of interest around 95 MeV. In the endpoint region the MIO rate varies as $(E_{\mu e} - E_{\mathrm{MIO}})^5$ and a resolution of 1–2 MeV (FWHM) is sufficient to keep MIO background under control (see Sect. 6.4 below). Since the MIO endpoint rises at lower Z great care has to be taken to avoid low-Z contaminations in and around the target.

Another background source is due to radiative muon capture (RMC) $\mu^-(A,Z) \to \gamma(A,Z-1)^*\nu_\mu$ after which the photon creates an e^+e^- pair either internally (Dalitz pair) or through $\gamma \to e^+e^-$ pair production in the target. The RMC endpoint can be kept below $E_{\mu e}$ for selected isotopes. For muonic gold the endpoint energy of electrons from RMC is 93.81 MeV. The process can be studied experimentally since it gives the same contribution to the positron distribution where it is the dominant process.

2.3 Pion induced background

Most low-energy muon beams have large pion contaminations. Pions may produce background when stopping in the target through radiative pion capture (RPC) which takes place with a probability of $O(10^{-2})$. Most RPC photons have energies above $E_{\mu e}$. As in the case of RMC these photons may produce background through $\gamma \to e^+e^-$ pair production.

Since pionic atoms decay promptly through the strong interaction RPC can be suppressed with the help of a veto counter in the beam or by using a pulsed proton beam. A third option which is the one chosen in these measurements is to keep the total number of π^- stopping in the target during the live time of the experiment below 10^{4-5}. To meet that requirement at most 1 out of 10^9 of the pions in the beam may reach the target. The pion suppression is then based on the different range distributions for pions and muons at given momentum. Figure 1 shows the probability of 52 MeV/c pions and muons to cross a CH_2 moderator of given thickness. As can be seen from the figure the mean range differs by about a factor two and range straggling can be neglected so perfect separation should be expected with an 8 mm thick CH_2 degrader. In practice the distributions are broadened by the finite momentum band transmitted by the beam line. Settings of the beam magnets and slits have to be carefully adjusted to minimize the tails in the pion range distribution. At the cost of $\approx 30\%$ loss in muon intensity the pion stops in the target could be suppressed to the required level. A simulation using the measured range distribution shows that about one in 10^6 pions cross the moderator. Since these particles are relatively slow 99.9% of them decay before reaching the target which is situated some 10 m further downstream.

RPC may produce background even when taking place in the moderator. The resulting electrons have $\approx 10\%$

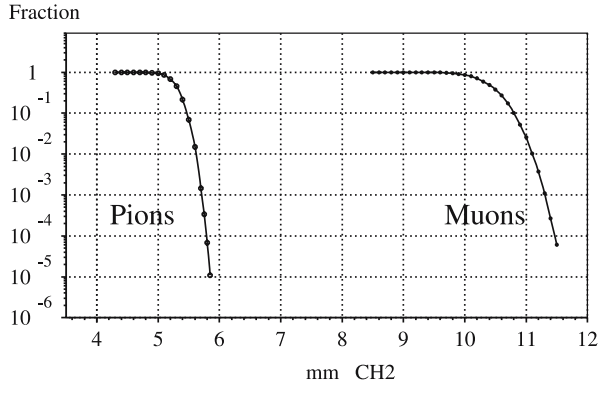

Fig. 1. Fraction of pions and muons with a momentum of 52 MeV/c that cross a CH_2 moderator as a function of the moderator thickness. GEANT [23] simulation

probability to be transported to the target from where they may scatter into the acceptance of the spectrometer. Pion decay in flight is another source of electrons in the beam.

2.4 Cosmic ray background

Cosmic rays (electrons, muons, photons) are a copious source of electrons with energies around ≈ 100 MeV. With the exception of $\gamma \to e^+e^-$ pair production in the target these events can be recognized by an incoming particle. In addition passive shielding and veto counters above the detection system help to suppress this background. From the analysis of data recorded over the years during extensive measuring periods without beam we found that it is possible to suppress this background below the level of 0.1 events at the cost of a loss in sensitivity of $O(10\%)$. See Sect. 6.2 for further details.

3 Experimental setup

The experiment was performed with the SINDRUM II solenoidal spectrometer at the PSI secondary beam line πE5. Figure 2 shows the experimental layout including proton beam, pion production target, secondary beam line, transport solenoid and SINDRUM II spectrometer. Vacuum is maintained all the way from the proton channel to the exit of the spectrometer. A thin window at the exit of πE5 keeps radio-active gases produced by the proton beam away from the detectors.

3.1 Muon beam

The 590 MeV proton beam has a time structure of 0.3 ns wide bursts every 19.75 ns. The πE5 secondary beam line extracts particles emitted in backward direction from the pion production target with a solid angle acceptance of 150 msr. Since practically all muons transmitted by the beam line originate from pion decay in the vicinity of the production target the delay between the time when the protons hit the production target and the time when a muon arrives at the beam exit is to good approximation given by the muon time of flight. As a result the muon momentum distribution can be deduced from the distribution of muon arrival times relative to the cyclotron rf signal. The experiment was performed at central momenta of 52 MeV/c and 53 MeV/c which is sufficiently low to avoid background from muon decay in flight.

The beam line is symmetric about the middle where the beam is focused in the vertical plane. Dispersive horizontal foci are found at two other positions. Slit systems at these locations (see Fig. 2) allow to define the momentum band. As has been discussed in Sect. 2.3 a narrow band is required for an efficient $\pi - \mu$ separation using the different range in matter. The momentum dispersion in the plane of the first horizontal (x) slit shown in inset a of Fig. 2 has been determined from the distributions of the muon time of flight for different slit positions. A momentum band of $\pm 2\%$ was selected during most of the data taking.

The beam spot at the end of the beam line was measured with the help of a slab of scintillating material viewed with a camera (inset b of Fig. 2). A further focus is found about 1 m behind the entrance of the transport solenoid, a 9 m long superconducting magnet operated at a field strength of 1.1 T. Here a lead collimator is situated with a diameter of 60 mm followed by an 8 mm thick CH_2 degrader which is used to remove pions from the beam (see Sect. 2.3). Because of the large momentum band behind the degrader and the many turns the muons make in the transport solenoid no beam focus exists inside the spectrometer. Still beam particles periodically return to the solenoid axis, i.e. every ≈ 65 cm for a typical momentum after the degrader of 35 MeV/c and for this reason the gold target was made in the form of a 65 cm long tube.

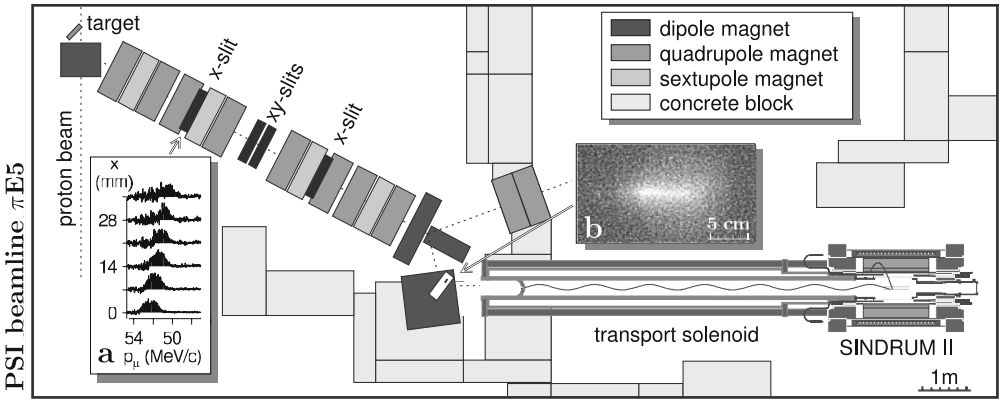

Fig. 2. Plan view of the experiment. The 1 MW 590 MeV proton beam extracted from the PSI ring cyclotron hits the 40 mm carbon production target (top left of the figure). The πE5 beam line transports secondary particles (π, μ, e) emitted in the backward direction to a degrader situated at the entrance of a transport solenoid connected axially to the SINDRUM II spectrometer. *Inset* **a**) shows the momentum dispersion measured at the position of the first slit system. The momentum was calculated from the flight time through the channel and the distributions show the increase when opening one side of the slit. *Inset* **b**) shows a cross section of the beam observed at the position of the beam focus

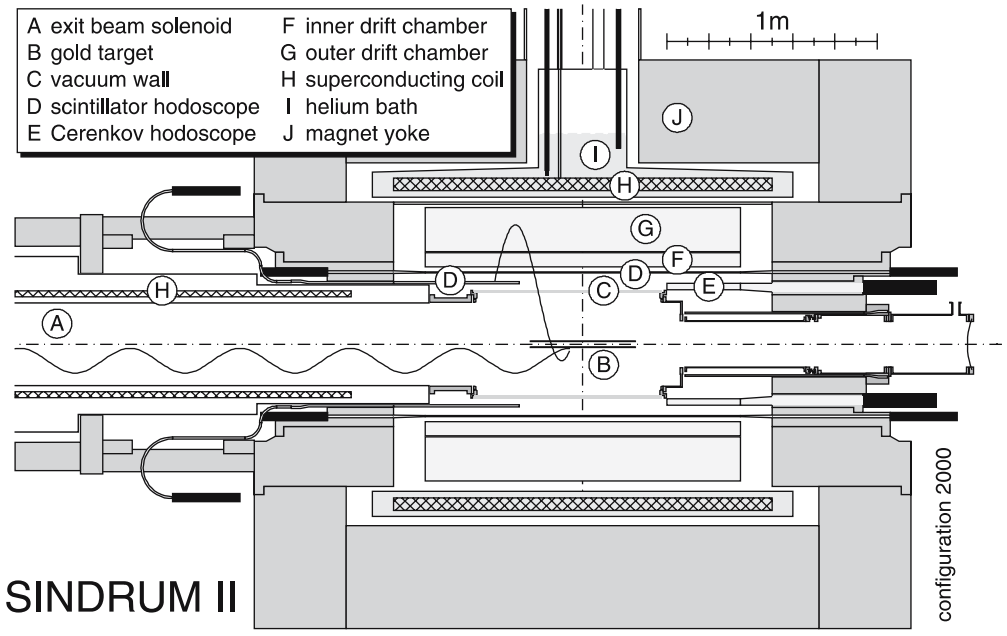

Fig. 3. The SINDRUM II spectrometer. Typical trajectories of a beam muon and a hypothetical conversion electron are indicated

3.2 SINDRUM II spectrometer

Figure 3 shows a vertical cross section through the SINDRUM II spectrometer in the configuration used for this experiment. Beam is entering from the solenoid (A in Fig. 3) on the left. The gold target (B) with a radius of ≈ 20 mm and a wall thickness of 75 mg/cm^2 was produced in a galvanic process to ensure the high purity required to suppress background from MIO in low and medium Z contaminations. Due to the lower muon binding energy such background reaches beyond $E_{\mu e}$ for gold.

As is illustrated in Fig. 3 hypothetical $\mu - e$ electrons are contained radially in the tracking region of 1.35 m diameter and 1.8 m length, making one or several turns before reaching an end-cap detector. The wall of the vacuum chamber inside the tracking region (C) consists of two concentric carbon fiber tubes separated by honeycomb and covered with aluminum foil giving a total thickness of only 0.325 g/cm^2 [19]. Two drift chambers DC1 and DC2 (F and G, respectively) were used to measure the helical trajectories. They extend radially between 37.6 and 44.1 cm and between 44.9 and 66.8 cm, respectively. In both tracking detectors the ionization electrons drift radially towards the amplification regions situated on the outside of the detectors. The spectrometer acceptance is defined by the requirement that the particles reach the DC1 sense wire plane at least once before crossing one of the end-cap hodoscopes. In this geometry half turns of the particle trajectories are recorded which minimizes the impact of multiple scattering on the momentum resolution.

The main tracking detector DC1 uses CO_2 -isobutane (70/30) as a drift gas. In this mixture electrons from ionization tracks have a drift velocity of ≈ 1 cm/μs at the 1 kV/cm drift field resulting in a moderate 6° Lorentz deflection. The 768 anode wires are situated at a radial position of 44.7 cm. Every second anode wire is a sense wire so 50% of the ionization electrons are collected. The wall separating DC1 and DC2 is made of low-density foam sandwiched between aluminized Kapton foils and has a density of only 35 mg/cm^2. To stabilize its position DC1 is kept at an overpressure of 1 mbar relative to DC2. The aluminum on the inside of the wall is divided into 4.4 mm wide helical strips which allows 3-dimensional track reconstruction. There are separate strips for the upstream and downstream halves of the detector (2×192 strips in total) oriented at $\pm 72°$ relative to the sense wires. The angle has opposite signs for the two hemispheres such that electrons never move in the direction along the strips. See [20] for further details.

The second tracking detector DC2 uses He-isobutane (85/15) as a drift gas. This gas mixture was chosen for its large radiation length of 1140 m with minimal impact on the momentum resolution of the spectrometer. About 30% of the ionization electrons are collected and amplified in 96 detector modules situated at a radial position of 65 cm.

Two plastic scintillator hodoscopes of 3 mm thickness (D) and a 3 cm thick plexiglass Čerenkov hodoscope (E) are used for triggering and for timing information. The main scintillator hodoscope situated just inside DC1 has 64 elements with photomultipliers at both ends. This detector is used in the trigger for data readout and off-line it defines the start time for the drift chambers and the direction of motion of the particle along the trajectory. Two end-cap hodoscopes are situated at both ends of the tracking region. These detectors are used for triggering and help to resolve ambiguities in the event reconstruction.

The procedures of the event reconstruction are described in Sect. 6.1 below. Figure 4 shows as an example the tracks left by a ≈ 100 MeV/c electron together with the reconstructed trajectory. The electron made two turns before reaching the Čerenkov hodoscope at the downstream end of the spectrometer. As will be discussed in Sect. 6.1 events with more than one turn can be reconstructed very reliably by testing the continuity of the trajectory between the first two turns.

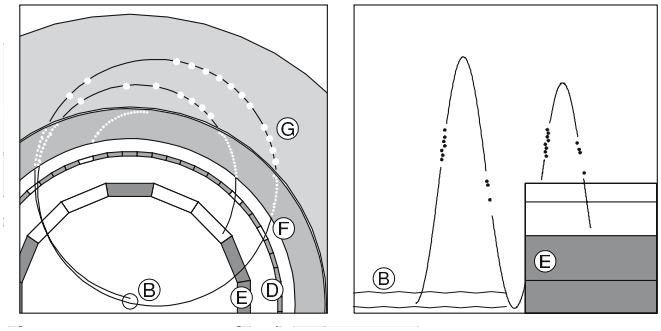

Fig. 4. Spectrometer tracks and reconstructed trajectory of a $\approx 100\,\mathrm{MeV/c}$ electron in projections perpendicular to (*left*) and along (*right*) the beam direction. See Fig. 3 for the definitions of the labels

3.3 Muon stop monitor

The number of muons stopping in the target was constantly monitored during actual data taking by observing the characteristic muonic gold X-rays passing through the superconducting coil of the spectrometer. A Ge(Li) detector was used for this purpose and a typical energy spectrum is shown in Fig. 5. The sensitivity of the monitor was determined by simulation and agrees within 3% with the results of a calibration with ^{137}Cs and ^{60}Co sources at three positions along the target.

4 Event simulation

Simulations of events of $\mu - e$ conversion, MIO and pion decay in flight were performed with GEANT [23]. Care was taken in the exact description of the geometry, in particular of the relative positions of the target, the active detector elements and the flanges of the inner vacuum tube. The various offsets were adjusted to best reproduce the measured distributions. Light propagation and attenuation in the scintillators and Čerenkov counters were properly taken into account and the discriminator threshold and time resolution of each individual detector channel was taken from the observed values.

As is illustrated in Fig. 4 the individual DC1 track segments have typically fifteen sense wire hits and roughly half of those have associated cathode signals which come in clusters of 2–3 neighbouring strips. The mean cathode efficiency per hit varied between 40% and 70% during the measurements. These variations were caused by changes in the settings for the electric field in the amplification region, adjustments of the discriminator thresholds and ageing effects in the drift gas. The simulation took these fluctuations into account. Dispersion in the drift velocity and signal loss caused by gas impurities lead to a deterioration of the position resolution and the single-hit cathode efficiency for larger drift times. These effects were included in the simulation as well.

The SINDRUM II magnetic field drops by about 10% on the downstream side of the spectrometer. A detailed magnetic field map was made with the detector components removed and the result was used in the simulation and event reconstruction.

The muon stop distribution over the target was adjusted to the measurement. In the simulation of MIO in gold the theoretical energy distribution for lead [24] was used, corrected for the 0.54 MeV shift in endpoint energy.

5 Data taking

5.1 Trigger for data readout

The trigger for data readout was based on the hit patterns in the three hodoscopes and the DC1 sense wires. Since the DC1 drift time reaches up to 7 μs the trigger decision was made in two steps. In the first step which took about 0.2 μs only prompt DC1 signals were considered. These correspond to track coordinates close to the sense wires. In the second step DC1 signals arriving 5–7 μs later were included. These signals correspond to track coordinates close to the inner wall of DC1.

Trigger conditions were defined both for circular and for straight trajectories. For the actual $\mu - e$ data taking a circular pattern was required as expected from the first turn of the trajectory of an electron or positron originating in

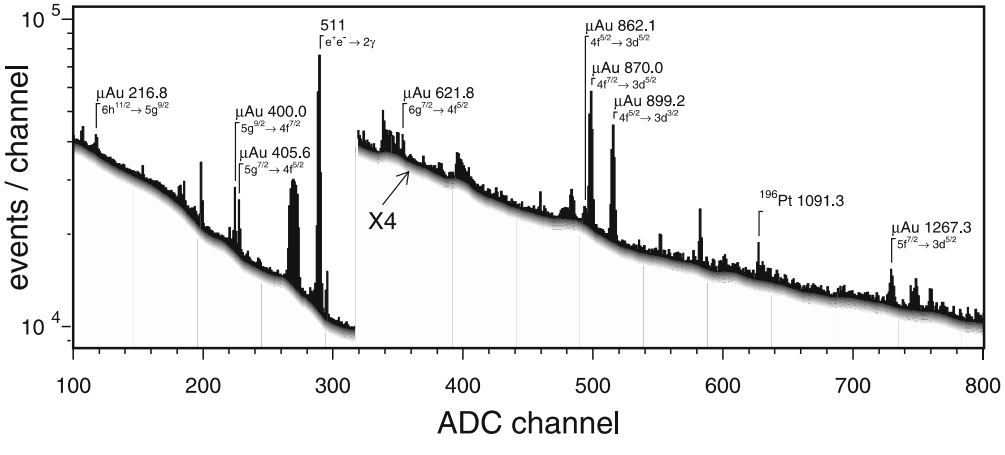

Fig. 5. X-ray spectrum accumulated during three hours of $\mu - e$ data taking. Energies and intensities were taken from [21, 22]

Table 1. Conditions of the five data sets

set nr.	beam (MeV/c)	SINDRUM field (T)	trigger	duration
1	$-52-53$	1.07	circle	81 days
2	off	1.07	straight	20 min / day
3	$+52$	0.54	circle	3 days
4	$-56-65$	1.07	circle	1 day
5	off	1.07	circle	16 days

the target and reaching the sense wire plane of DC1 at least once before crossing an endcap detector. A second trigger pattern was implemented corresponding to straight trajectories crossing DC1 twice. This trigger condition selects events with high energy cosmic muons which were used for the calibration of the DC1 drift time.

5.2 Data samples

Table 1 lists the different beam and trigger conditions at which data have been recorded. The following five data sets were accumulated:

- Set 1 is the main event sample used for the actual search for $\mu - e$ conversion. The magnetic field was optimized for largest geometric acceptance at 95 MeV/c. In addition to electrons the sample contains positrons which allow us to study background pocesses with intermediate photons.
- Set 2 contains events with high-momentum muons from cosmic radiation which leave almost straight tracks in DC1. These events recorded during 20 min every day with beam switched off were used to calibrate the relation between drift time and position (see Sect. 6.1 below). The calibration varies in time since the drift velocity depends on pressure and temperature which were not stabilized in the experiment.
- Set 3 contains mostly $\mu^+ \to e^+\nu\overline{\nu}$ decays used to calibrate the magnetic field and check the momentum resolution. The spectrometer field was reversed and scaled down to give at the endpoint energy approximately the same trajectories as expected for $\mu - e$ events in set 1. The scaling factor was measured with a Hall probe.
- Set 4 was used to study background from pions stopping in the target. The pion stop rate rises steeply between 53 and 65 MeV/c beam momentum which corresponds to a doubling of the mean range for pions. From these data it was concluded that background induced by π^- reaching the target can be ignored at the beam momentum selected for set 1.
- Set 5 was used to study cosmic ray background.

6 Event reconstruction and selection

In the offline analysis events are selected with electron or positron trajectories originating in the target and reaching the DC1 sense wire plane at least once before eventually crossing an endcap detector. Since the region of interest is situated at the endpoint of a steeply falling background care has to be taken to minimize high-energy tails in the response function caused by errors in the trajectory reconstruction. In the spirit of a "blind analysis" selection criteria are optimized for the complete sample including both electrons and positrons and without knowledge of the precise energy. Cuts aiming at rejection of cosmic ray background are taken from earlier measurements.

6.1 Trajectory reconstruction

Particle trajectories are reconstructed in four steps. First DC1 track elements are sought independently in the drift time patterns of both the sense wires and the cathode strips. In a second step sense wire and cathode track elements are combined pairwise such that the total number of coincident signals from sense wires and cathode strips in the event is maximized. The method is unbiased in the sense that no attempt is made yet to find the helical trajectory expected for the events of interest.

In a third step the drift times observed from DC1 sense wires are converted into $r \times \varphi$ coordinates. The DC1 isochrons are approximated by arcs. As a result of the $1/r$ dependence of the drift field isochron radius, drift velocity and Lorentz deflection angle all depend on drift distance. The relation between drift time and position is described with the help of six parameters which are fit to the high momentum trajectories from data set 2 (see Sect. 5.2). The resulting 3-dimensional track elements have to point at a hodoscope hit at a location consistent with the time difference observed at the two hodoscope ends. As can be seen in Fig. 6 a very strong correlation can be observed between

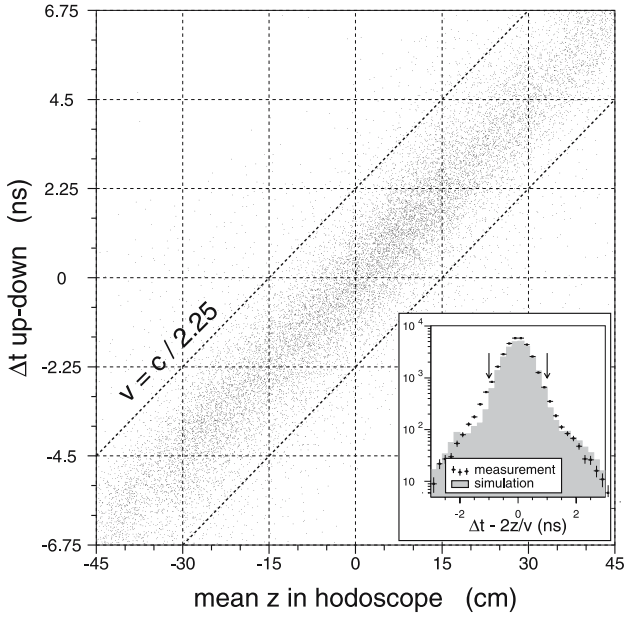

Fig. 6. Correlation of the time difference observed at the two hodoscope ends and the track coordinate at the hodoscope. The distribution indicates an effective velocity of scintillation light of $c/2.25$. The *inset* shows the projection along the diagonal. Cuts used in the analysis are indicated

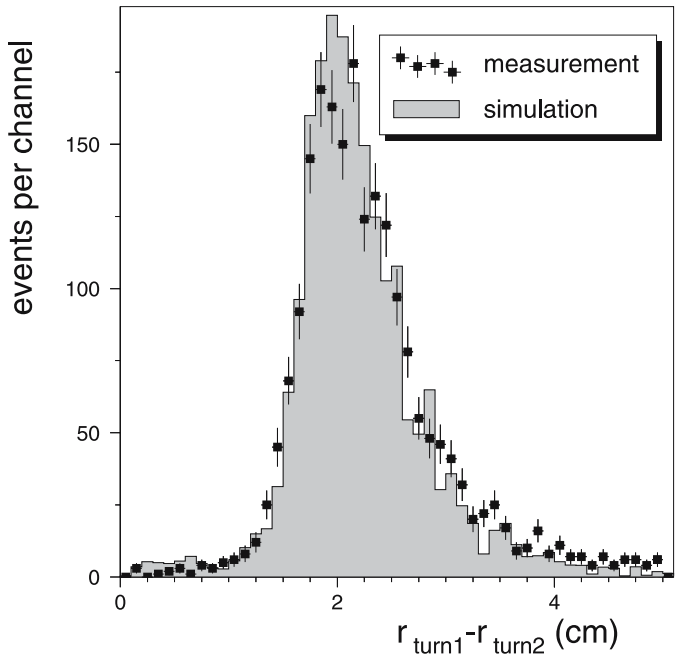

Fig. 7. Change in radius of the helical trajectory between the first two turns

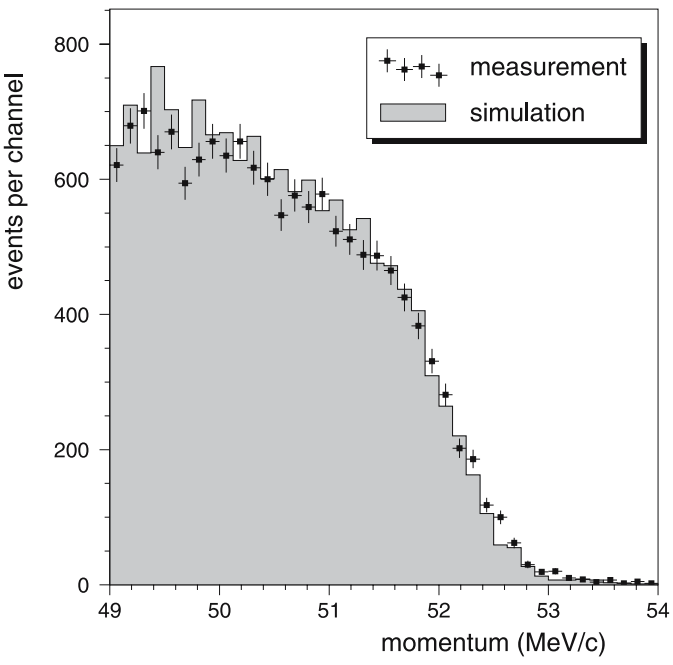

Fig. 8. Endpoint region of the positron momentum spectrum from the decay $\mu^+ \to e^+\nu\overline{\nu}$

these quantities demonstrating the very low level of reconstruction errors.

In a fourth step pairs of track elements are combined into turns and trajectories are fit to each of them independently. Multiple scattering is taken into account. In the case of events with single turns it is required that at least 20% of the DC1 hits have cathode information. In case of several turns they are ordered based on decreasing trajectory radius and increasing hodocope timing and trajectory continuity is required between the first two turns. Figure 7 shows as an example a histogram of the difference in radius of the first two turns. The observed peak is shifted to ≈ 2 cm by energy loss mainly in the hodoscope and the wall of the vacuum chamber which are traversed twice in between the turns. The left side of the peak shows a 10%–90% rise within 3 mm which translates into a resolution in transverse momentum around 1% FWHM.

A check of the momentum resolution of the spectrometer can be made by observing the endpoint region of the positron momentum distribution for the $\mu^+ \to e^+\nu\overline{\nu}$ decay (see Fig. 8). By comparing measured and simulated distributions the central value of the spectrometer field was calibrated which results in a value of $\mathrm{B} = 1.069 \pm 0.001$ T for μe data taking.

Figure 9 shows distributions of the trajectory origin after suppression of cosmic ray background (see Sect. 6.2 below) and the contours used for the selection of events with particles emitted from the target.

6.2 Cosmic-ray induced background

Cosmic ray background has been studied extensively in earlier years so the rejection criteria could be fixed before the start of the actual measurement. Three classes of

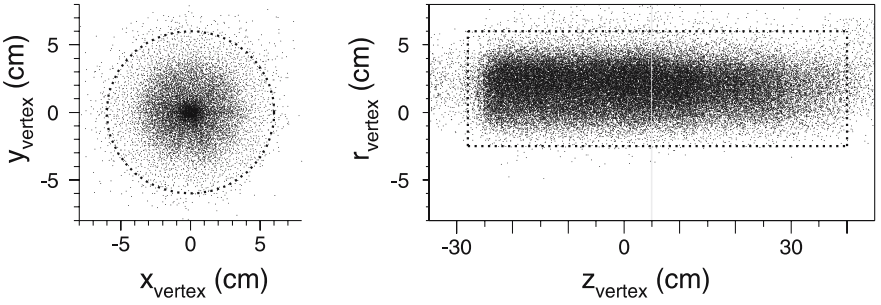

Fig. 9. Spatial distributions of the starting point of the first turn defined as the location on the trajectory closest to the beam axis. Negative values of r correspond to the situation in which the particle moves around the beam axis. A clean signal of target correlated events is seen. Similar to the situation observed in Fig. 7 the centroid of the r distribution is shifted away from zero because of the energy loss before DC1 is reached. The contours indicate the cuts applied in the analysis

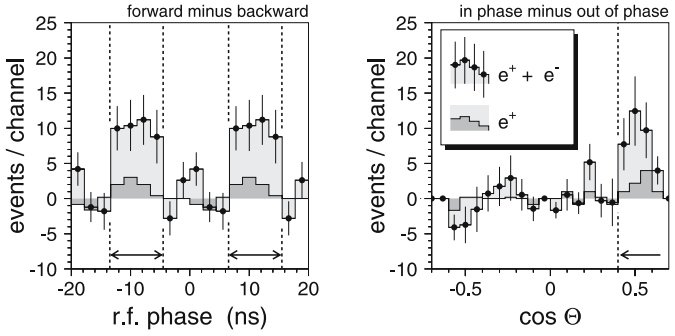

Fig. 10. Prompt beam induced background. Electron and positron events were selected with total momentum above 87 MeV/c but outside the main signal region 92.5–95.5 MeV/c. *Panel a*: spectrometer timing relative to the 50.6 MHz cyclotron rf signal. Time differences with respect to both the previous and the next rf bucket are incremented. Shown is the difference between the distributions with $\cos\theta > 0.4$ and $\cos\theta < -0.4$. *Panel b*: $\cos\theta$ distribution. Shown is the distribution corresponding to the phase enhancement by the pion induced events. The *arrows* indicate the region populated by pion induced events. See the text for a discussion of the nature of these events

cosmic background can be distinguished. Most common is a high momentum muon which knocks out an atomic electron either from the target or from the vacuum chamber. These events, observed typically once every second, are recognized by the signals left by the high momentum muon. In the second class of events the electron enters the tracking region from the outside. The vast majority of these events is recognized since the reconstructed trajectory does not originate in the target. The rest of these events can be rejected on the basis of an early signal in one of the hodoscopes. In the third type of event a photon from a cosmic ray shower creates an asymmetric e^+e^- pair in the target. This background is suppressed very effectively by the magnet return yoke on top of the spectrometer and by 10 cm lead shields on the sides. Some photons, however, penetrate through a hole in the yoke containing the liquid Helium supply lines (see Fig. 3). Thanks to the low-mass target this background is reduced by an order of magnitude compared to our earlier measurements on lead [26]. Still a few events are expected so the $\approx 4\%$ acceptance cut removing this component was maintained.

6.3 Pion induced background

Potential pion background has been discussed in Sect. 2.3. Pion stops in the target have been reduced to a negligible level by careful beam tuning so what remains are radiative pion capture (RPC) in the degrader and decay in flight in the region just before the degrader. Since these processes are associated with large angle scattering off the target the events are peaked in forward direction and show a time correlation with the cyclotron rf signal. RPC background is charge symmetric after taking into account that for energies around 100 MeV scattering cross sections on gold are typically twice larger for positrons than for electrons [25]. Simulation shows that decay in flight is dominantly $\pi^- \to e^-\overline{\nu}_e$ shortly before the pion would have reached the moderator. $\mathcal{O}(10)$ background events are expected with a flat energy distribution between 80 and 100 MeV. The decay chain $\pi^- \to \mu^-\overline{\nu}_\mu$, $\mu^- \to e^-\nu_\mu\overline{\nu}_e$ has a similar yield but the energy distribution falls steeply and is for all energies negligible compared to MIO.

As is illustrated in Fig. 10 there is indeed a beam correlated signal which is strongly peaked in the forward direction and which does contain more electrons than positrons. The observed time spread is ≈ 10 ns explained mainly by the momentum spread in the beam.

To cope with π^- induced background two event classes have been introduced based on the values of polar angle and rf phase:

- Class 1 contains events with $\cos\theta < 0.4$ or $|t_{\rm rf} - 10\,{\rm ns}| > 4.5$ ns which are practically free of pion induced background.
- Class 2 contains events with $\cos\theta > 0.4$ and $|t_{\rm rf} - 10\,{\rm ns}| < 4.5$ ns which are contaminated by pion induced background.

6.4 Single-event sensitiviy

The single-event sensitivity for $\mu - e$ conversion $\mathrm{S}_{\mu e}$ which is defined as the value for the branching ratio $B_{\mu e} \equiv \Gamma(\mu^-\mathrm{Au} \to e^-\mathrm{Au}_{\mathrm{g.s.}})/\Gamma_{\mathrm{capture}}(\mu^-\mathrm{Au})$ corresponding to an expectation value of one event in one of the two final event classes described above can be calculated using

$$\mathrm{S}^i_{\mu e} = \frac{1}{\mathrm{N}_\mu \cdot \mathrm{R}_{\mathrm{capt}} \cdot \Omega \cdot \epsilon_i}\,, \quad i = 1, 2 \tag{2}$$

with $\mathrm{N}_\mu = (4.37 \pm 0.32) \times 10^{13}$ the total number of muons that stopped in the gold target during the live time of the measurement (see Sect. 3.3), $\mathrm{R}_{\mathrm{capt}} = (97.17 \pm 0.02)\,\%$ [14] the probability for nuclear muon capture in muonic gold, $\Omega = 0.44$ the spectrometer acceptance and ϵ_i the efficiency factor for each of the two event classes accounting for various losses associated with the detector efficiencies, the trigger, event reconstruction and event selection. The evaluation of $\epsilon_1 = 0.21 \pm 0.01$ and $\epsilon_2 = 0.015 \pm 0.002$ was done with the help of the event simulation (see Sect. 4) where most parameters affecting the sensitivity were adjusted to the measurement. When studying the nature of the overall efficiency factor $\epsilon_1 + \epsilon_2 = 0.225$ one finds that detector inefficiencies, $r \times \varphi$ track reconstruction, z reconstruction, cosmic background suppression and event selection introduce similar losses of $\approx 20\%$ each. As a result $\mathrm{S}^1_{\mu e} = (2.5 \pm 0.2) \times 10^{-13}$ and $\mathrm{S}^2_{\mu e} = (3.6 \pm 0.4) \times 10^{-12}$.

7 Likelihood analysis

The search for $\mu - e$ conversion is based primarily on the analysis of the electron momentum which is the only observable that allows to distinguish the signal from muon

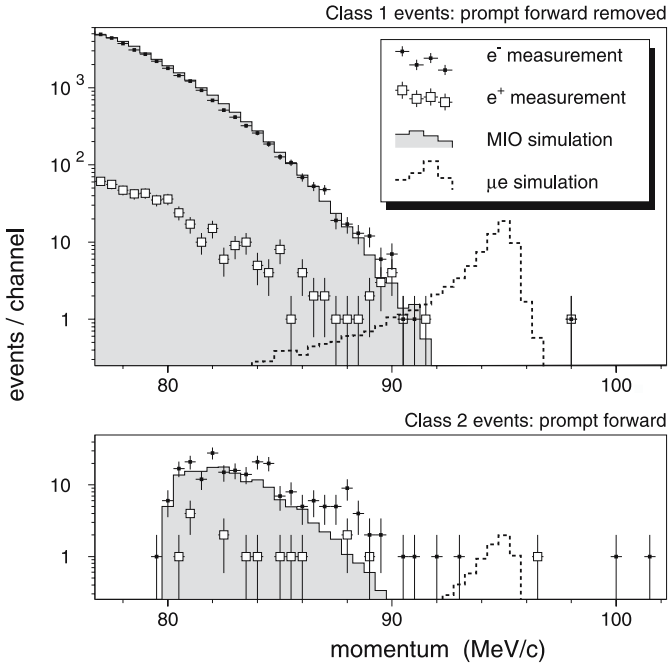

Fig. 11. Momentum distributions of electrons and positrons for the two event classes. Measured distributions are compared with the results of simulations of muon decay in orbit and $\mu - e$ conversion

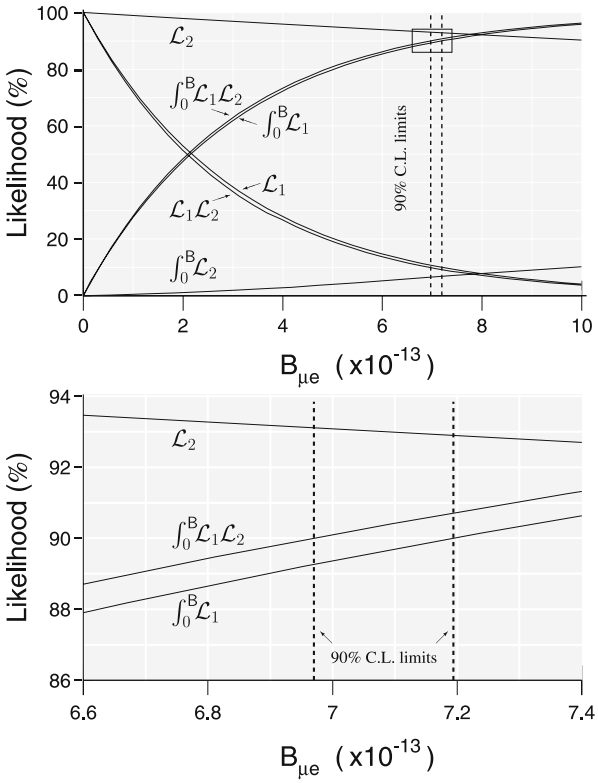

Fig. 12. $B_{\mu e}$ likelihood distributions for the two event classes and their combination. The distributions are arbitrarily normalized to 1 at $B_{\mu e} = 0$ where they peak. Also shown are the integral distributions normalized to 1 over the full region. The *lower panel* gives an enlarged view of the region where the 90% confidence level is reached

decay in orbit (MIO) which is the dominant source of background. Figure 11 shows momentum spectra of electrons and positrons for the two event classes introduced in Sect. 6.3. In general the electron distribution of sample 1 is well described by muon decay in orbit. Whereas no events are observed with energies expected for $\mu - e$ conversion at higher energy an electron and a positron event have been found. Since cosmic ray background contains much more electrons than positrons these events are most likely caused by pions. In sample 2 the electron distribution shows in addition to muon decay in orbit a more or less flat component as expected from pion induced background. One should conclude that the measurement shows no indication for $\mu - e$ conversion. The corresponding upper limit on $B_{\mu e}$ has been obtained with the help of a likelihood analysis of the momentum distributions shown in Fig. 11 which avoids arbitrary cut parameters. The following four contributions were taken into account:

- muon decay in orbit,
- $\mu - e$ conversion,
- a contribution taken directly from the observed positron distribution describing processes with intermediate photons such as radiative muon capture,
- a flat component resulting from $\pi^- \to e^- \overline{\nu}_e$ in flight or some remaining cosmic ray background.

The likelihood analysis results in likelihood distributions for the expectation values for the number of events from each of these contributions which are the basis for the calculation of the upper limit on $B_{\mu e}$ for any given confidence level.

7.1 Results

Whereas the shape of the electron momentum distribution is well reproduced by the MIO simulation the number of events found in the likelihood analysis is about 10% less than expected from the total number of stopped muons (see Sect. 3.3 and Sect. 6.4). Although this discrepancy is not significant we decided to normalize the measurements to the MIO events, i.e. raise the estimated μe single event sensitivities given in Sect. 6.4 to $S^1_{\mu e} = (2.8 \pm 0.2) \times 10^{-13}$ and $S^2_{\mu e} = (3.7 \pm 0.2) \times 10^{-12}$ where the errors are reduced since most of the uncertainties cancel in the normalization procedure.

Figure 12 shows the resulting likelihood distributions $\mathcal{L}(B_{\mu e})$ for both event classes separate ($\mathcal{L}_1$ and $\mathcal{L}_2$) and for the total ($\mathcal{L}_{\rm tot} = \mathcal{L}_1 \times \mathcal{L}_2$). Also shown in Fig. 12 are the distributions of the integrals $\int_0^B \mathcal{L}\,{\rm d}B$ normalized to their asymptotic value $\int_0^\infty \mathcal{L}\,{\rm d}B = 1$. The upper limit at 90% confidence level $B^{90\%C.L.}_{\mu e}$ is thus given by:

$$\int_0^{B^{90\%C.L.}_{\mu e}} \mathcal{L}_{\rm tot}\,{\rm d}B = 0.9\,, \tag{3}$$

which leads to the following result for the branching ratio of $\mu - e$ conversion in muonic gold relative to the nuclear

capture probability:

$$B_{\mu e}^{\mathrm{Au}} < 7 \times 10^{-13} \quad 90\%\, C.L. \tag{4}$$

This limit is more stringent by two orders of magnitude than the best previous limit on a heavy target [26]. It is the final result of the research program on rare π and μ decays with the SINDRUM I and II spectrometers at PSI. The search for LFV in rare muon decays is continued at PSI by the MEG collaboration [27] aiming at a sensitivity of 10^{-13} for the $\mu \to e\gamma$ decay.

References

1. R.D. McKeown, P. Vogel, Phys. Rept. **394**, 315 (2004)
2. A. van der Schaaf, Prog. Part. Nucl. Phys. **31**, 1 (1993)
3. T.S. Kosmas, G.K. Leontaris, J.D. Vergados, Prog. Part. Nucl. Phys. **33**, 397 (1994)
4. Y. Kuno, Y. Okada, Rev. Mod. Phys. **73**, 151 (2001)
5. J. Aysto et al., Physics with low-energy muons at a neutrino factory complex, arXiv:hep-ph/0109217, in: A. Blondel et al., ECFA/CERN studies of a European neutrino factory complex, CERN-2004-002.
6. S. Eidelman et al., Phys. Lett. **B 592**, 1 (2004)
7. BABAR Collaboration, B. Aubert et al., Phys. Rev. Lett. **95**, 041 802 (2005)
8. BaBar Collaboration, B. Aubert et al., Phys. Rev. Lett. **95**, 191 801 (2005)
9. BABAR Collaboration, B. Aubert et al., Phys. Rev. Lett. **96**, 041 801 (2006)
10. MEGA Collaboration, M. Ahmed et al., Phys. Rev. D **65**, 112 002 (2002) [arXiv:hep-ex/0111030]
11. SINDRUM Collaboration, U. Bellgardt et al., Nucl. Phys. B **299**, 1 (1988)
12. W. Bertl et al., Prepared for International Europhysics Conference on High-Energy Physics (HEP 2001), Budapest, Hungary, 12–18 Jul 2001.
13. A. van der Schaaf, J. Phys. G **29**, 1503 (2003)
14. T. Suzuki et al., Phys. Rev. C **35**, 2212 (1987)
15. A. Czarnecki, W.J. Marciano, K. Melnikov, AIP Conf. Proc. **549**, 938 (2002)
16. T.S. Kosmas, I.E. Lagaris, J. Phys. G **28**, 2907 (2002)
17. R. Kitano, M. Koike, Y. Okada, Phys. Rev. D **66**, 096 002 (2002) [arXiv:hep-ph/0203110]
18. T.S. Kosmas, J.D. Vergados, O. Civitarese, A. Faessler, Nucl. Phys. A **570**, 637 (1994)
19. E.A. Hermes, H.P. Wirtz, F. Rosenbaum, Nucl. Instrum. Meth. A **413**, 185 (1998)
20. M. Grossmann-Handschin et al., Nucl. Instrum. Meth. A **327**, 378 (1993)
21. B. Robert-Tissot, "Analyse de Transitions Muoniques dans l'Atome d'^{197}Au", PhD thesis, Univ. Fribourg, 1975, Switzerland.
22. F.J. Hartmann, R. Bergmann, H. Daniel, H.J. Pfeiffer, T. Von Egidy, W. Wilhelm, Z. Phys. A **305**, 189 (1982)
23. GEANT, Detector Description and Simulation Tool, CERN Program Library Long Writeup W5013. GEANT Version 3.21 is used with the default values for all parameters
24. R. Watanabe et al., Atom. Data Nucl. Data Tab. **54**, 165 (1993)
25. C.R. Fischer, G.H. Rawitscher, Phys. Rev. **B377**, 135, (1964)
26. SINDRUM Collaboration, W. Honecker et al., Phys. Rev. Lett. **76**, 200 (1996)
27. PSI proposal R-99-05